CrystEngComm

PAPER

View Article Online
View Journal | View Issue

Cite this: *CrystEngComm*, 2025, **27**, 6184

Sustainable mechanochemical approach for the selective synthesis of multicomponent organic solids: real-time *in situ* insights

Torvid Feiler,[ab] Franziska Emmerling *[ab] and Biswajit Bhattacharya *[a]

Crystalline multicomponent organic solids (MOSs) such as cocrystals and ionic cocrystals hold immense potential in diverse functional applications, ranging from pharmaceuticals to optoelectronics. However, conventional solution-based crystallization methods often result in polymorphic mixtures and lack precise control over product composition. Herein, we report a comparative investigation of solution crystallization *versus* mechanochemical synthesis for constructing MOSs from 9-anthracenecarboxylic acid (ACA) and 4,4′-bipyridine (BPY). Solution-based approaches consistently yielded concomitant formation of neutral cocrystal (CC) and ionic cocrystal (ICC) forms, regardless of the solvent used. The resulting multicomponent solids were comprehensively characterized using a combination of single crystal X-ray diffraction, powder X-ray diffraction, Fourier-transform infrared spectroscopy, differential thermal analysis, and thermogravimetric analysis. In contrast, mechanochemical methods, including neat grinding (without solvent) and liquid-assisted grinding (with minimum solvent), enabled selective formation of either a phase pure CC or ICC form. Less polar and nonpolar organic solvents favor the kinetic CC, while polar water promotes formation of the thermodynamically stable ICC. Time-resolved *in situ* powder X-ray diffraction (TRIS-PXRD) captures the dynamic evolution of solid-state phases and reveals the complete transformation of the CC into ICC under neat grinding or water-assisted conditions. This study highlights the powerful role of mechanochemistry and *in situ* monitoring in steering solid-state reactivity and offers a sustainable pathway for the targeted and scalable synthesis of pure multicomponent organic materials.

Received 2nd July 2025,
Accepted 13th August 2025

DOI: 10.1039/d5ce00663e

rsc.li/crystengcomm

Introduction

Crystalline multicomponent organic solids (MOSs), including cocrystals, salts, and solvates, have emerged as a transformative class of materials with broad applicability across diverse scientific domains.[1–6] These solids self-assemble from two or more distinct molecular entities in precise stoichiometric ratios, driven by noncovalent interactions such as hydrogen bonding, halogen bonding, π–π stacking, and charge-transfer interactions.[7–9] The resulting new materials often exhibit enhanced physicochemical and functional properties, surpassing those of their individual components due to synergistic effects at the molecular level.[10–12] In the pharmaceutical sector, cocrystallization has proven to be a powerful strategy for optimizing drug performance by improving stability, solubility, and bioavailability.[13–15] Notably, at least eight pharmaceutical cocrystals have already received regulatory approval, with many more advancing through the clinical pipeline.[16] Beyond pharmaceuticals, multicomponent organic solids have been harnessed to elevate the performance of nonlinear optical materials,[17,18] molecular semiconductors,[19,20] and energetic materials, including explosives,[21] propellants,[22] and pyrotechnics.[23] As research in this field continues to advance, MOSs are poised to drive the next generation of high-performance functional materials, offering unprecedented tunability and versatility.[5,8,24]

Conventionally, MOSs are prepared by solvent-based crystallization methods, which rely on large volumes of environmentally hazardous solvents and prolonged reaction times.[25,26] These methods are often constrained by poor scalability and reproducibility, posing significant challenges for large-scale production.[27] Additionally, solvent-mediated synthesis can result in polymorphic variations or uncontrolled stoichiometry, leading to unintended solid forms that compromise the physical and chemical properties of the final material.[28–31] These limitations underscore the urgent need for more sustainable and controllable synthetic

[a] *Department of Materials Chemistry, Federal Institute for Materials Research and Testing (BAM), Richard-Willstätter-Str. 11, Berlin 12489, Germany. E-mail: franziska.emmerlin@bam.de, biswajit.bhattacharya@bam.de*
[b] *Department of Chemistry, Humboldt-Universität zu Berlin, Brook-Taylor-Str. 2, 12489 Berlin, Germany*

approaches.[32] In this regard, environmentally benign mechanochemical synthesis, in which reactants are transformed into products through grinding, milling, or shearing, often without solvents or with only minimal solvent use, offers an attractive alternative to conventional solution-based synthesis.[33–36] This solvent-free approach offers unparalleled selectivity and control over the stoichiometric composition of the final product, minimizing undesired polymorphic or multicomponent variations.[37] Mechanochemical techniques have already been widely demonstrated for the efficient and rapid synthesis of various functional materials, including MOSs, porous frameworks, composites, and biomolecules.[38–44] Beyond its environmental and scalability advantages, mechanochemical synthesis enables real-time monitoring of solid-state transformations. By leveraging time-resolved *in situ* powder X-ray diffraction (TRIS-PXRD) and spectroscopy, researchers can probe local geometries, phase compositions, and crystallinity changes in intermediates and final products.[45–47] A deeper understanding of these mechanistic pathways facilitates the targeted and bulk-scale production of functional materials with tailored properties, unlocking new possibilities for high-performance applications.[48–53]

Herein, we have systematically investigated the formation of multicomponent organic solids from 9-anthracenecarboxylic acid (ACA) and 4,4′-bipyridine (BPY) using solution crystallization and mechanochemical approaches. ACA and BPY were selected for cocrystallization due to their complementary hydrogen bonding features. BPY contains two nitrogen atoms that act as effective hydrogen bond acceptors, while ACA possesses a single carboxylic acid group, which serves as a reliable hydrogen bond donor. To optimize these interactions and promote the formation of predictable supramolecular assemblies, a 2 : 1 molar ratio of ACA to BPY was used. Solution-based crystallization consistently yielded two concomitant MOSs, such as cocrystal ACA–BPY (CC) and molecular ionic cocrystal ACA^-–BPY^+–ACA (ICC), regardless of the solvents employed. In contrast, mechanochemical synthesis under dry conditions or with minimal solvent produced either a pure CC or ICC, depending on the choice of solvent during grinding. Furthermore, we employed real-time *in situ* powder X-ray diffraction (PXRD) to monitor the mechanochemical synthesis of both multicomponent systems, enabling a detailed analysis of their formation pathways. This approach provides critical insights into the mechanistic aspects of mechanochemical formation of MOSs, offering new perspectives for the controlled and scalable synthesis of these functional materials.

Experimental section

Materials

9-Anthracenecarboxylic acid and 4,4′-bipyridine were purchased from Sigma-Aldrich. All chemicals and solvents were used as delivered without purification.

Preparation of single crystals of cocrystal ACA–BPY (CC) and molecular ionic cocrystal ACA^-–BPY^+–ACA (ICC)

ACA (222 mg, 1 mmol) and BPY (78 mg, 0.5 mmol) in a 2 : 1 stoichiometric ratio were ground in a mortar and pestle with a few drops of MeOH for approximately 5 minutes, a process repeated thrice to ensure thorough mixing. Subsequently, the resulting dry powder is dissolved in hot methanol (45 °C, 25 ml). After a 4 day duration, plate and needle-shaped single crystals of both MOSs are harvested. Both the single crystals were analyzed by single-crystal X-ray diffraction. We have also explored the use of various organic solvents, including ethanol, acetonitrile, tetrahydrofuran, and dichloromethane, for solvent crystallization experiments.

Preparation of the CC and ICC *via* mechanochemical synthesis

In a typical milling experiment, ACA (222 mg, 1 mmol) and BPY (78 mg, 0.5 mmol) in a 2 : 1 stoichiometric ratio were taken into a milling jar (steel, 10 ml) along with two stainless steel balls (10 mm, 4 g). The mixture was milled at 50 Hz without using any solvent (neat grinding) and using different organic solvents such as water, methanol, and THF. The obtained powder was immediately taken to the powder X-ray diffraction measurements. For the TRIS-PXRD measurements during the ball milling experiment, a reduced reactant quantity (one-fourth of the standard amount) was employed. The milling was performed in a custom-designed PMMA jar, featuring hemispherical steel ends with a diameter of 12 mm, to ensure optimal mixing and diffraction signal clarity.

Analytical methods

Single crystal X-ray diffraction. The single crystal X-ray diffraction (SCXRD) data for both multicomponent crystals, individually mounted on a glass tip, were collected using a Bruker D8 Venture system equipped with graphite-monochromatic Mo Kα radiation (λ = 0.71073 Å). Data reduction was carried out using the Bruker AXS SAINT[54] and SADABS[55] software packages. Structural determination was performed employing SHELXS 2018 (ref. 56) *via* direct methods, followed by successive Fourier and difference Fourier synthesis. Full matrix least-squares refinements were conducted on F^2 utilizing SHELXL-2018,[56] incorporating anisotropic displacement parameters for all non-hydrogen atoms. Additional calculations were executed using SHELXS 2018 (ref. 56) and SHELXL 2018.[56] Mercury v3.6 was utilized for visualization and figure drawing of the structures. Hydrogen atoms attached to oxygen were located using the electron density map, while all hydrogen atoms attached to carbon were restrained to ideal positions.

***Ex situ* powder X-ray diffraction.** All mechanochemically treated powders were analyzed using powder X-ray diffraction (PXRD) immediately after milling. The milled powders were carefully loaded onto standard PVC sample holders, which were then mounted on the diffractometer for analysis. PXRD data were collected using a Bruker D8 Advance diffractometer

(Bruker AXS, Germany) operating in Bragg–Brentano geometry. A Lynxeye XE-T energy-dispersive point detector was employed in conjunction with Cu-Kα_1 radiation (λ = 1.540566 Å). Diffraction patterns were recorded over a 2θ range of 5° to 60°, with a step size of 0.02° and a counting time of 0.6 s per step.

Fourier transform infrared spectroscopy (FTIR). FTIR spectra were obtained employing a Nicolet FT-IR NEXUS (Thermoelectron) equipped with a Diamant-ATR-Golden Gate unit. Data were detected with a DTGS KBr detector. The spectra were collected over the range of 200–4000 cm^{-1} with a spectral resolution of 4 cm^{-1}.

Thermal analysis. Differential thermal analysis (DTA) was conducted using a TAG24 thermoscale (Setaram). The measurements were executed within an open platinum cup under a continuous Ar–air flow, with a heating rate of 10 K min^{-1} across the temperature range from 25 °C to 300 °C.

***In situ* PXRD.** *In situ* PXRD measurements were conducted at the μSpot beamline situated within the BESSY II electron storage ring, operated by the Helmholtz-Zentrum Berlin für Materialien und Energie. A beam size of 100 μm was employed at a photon energy of 17.44 keV, using a double crystal monochromator (SI 111). To prevent double reflections, the milling jar was strategically positioned such that the beam traversed approximately 50 μm within the jar walls. Scattered intensities were collected using a two-dimensional X-ray detector (Eiger 9 M, HPC 3110 × 3269 pixels, with a pixel size of 75 × 75 μm) with a time resolution of 5 s and a sample-detector distance of 233.5 mm. The acquired scattering images underwent processing using the DPDAK software. Then, background subtraction was performed on the resulting patterns using a custom-made Python script. Analysis, processing, and visualization of the data were carried out using Origin software (Version 2021, OriginLabs Corporation, Northampton, MA, USA).

Results and discussion

Liquid-assisted grinding of 9-anthracenecarboxylic acid (ACA) together with 4,4′-bipyridine (BPY) in a 2 : 1 ratio followed by slow evaporation crystallization from methanol readily afforded thick plate (CC) and needle-shaped (ICC) crystals concomitantly (Fig. 1). Other common organic solvents such as ethanol, THF, DCM, and ACN also produced both crystals concomitantly, only the quantity of both crystals has changed with solvents. Crystallization of pure form through the solvent method has never been successful with single or a mixture of solvents. The plate-type crystals could be easily separated from the needles. Both the crystals were characterized by FTIR, DTA-TG, and SCXRD. In FTIR spectra, characteristic C=O stretching vibration of ACA at 1673 cm^{-1} is blue-shifted to 1697 cm^{-1} (for the CC) and 1673 cm^{-1} (for the ICC), which signifies the formation of multicomponent solids (Fig. S1). The DTA thermograms of both the solids displayed a single endothermic peak up to the melting point, which suggests no phase transition before melting. The CC exhibited a sharp endothermic peak at approximately 188 °C, corresponding to its melting point. In contrast, the ICC displayed a similarly sharp melting endotherm at a slightly elevated temperature of 190 °C, reflecting its enhanced thermal stability relative to the CC (Fig. S2).

Crystal structures of ACA–BPY (2 : 1)

Single-crystal X-ray analysis revealed that cocrystal ACA–BPY (CC) crystallizes in the monoclinic space group $C2/c$ (Z = 8) with one ACA and half of the BPY molecules in the asymmetric unit (Fig. S3). Here, each BPY molecule interacts with two ACA molecules through N–H···O hydrogen bonds [O···N (Å), θ/°: 2.6024(15), 177; Table S1] to form a three component supramolecular assembly (Fig. 2a). Each three-component supramolecular assembly is connected with six adjacent similar assemblies *via* C–H···O interactions [O···C (Å), θ/°: 3.4718(18), 156; 3.544(3), 163] (Table S1; Fig. 2b). The

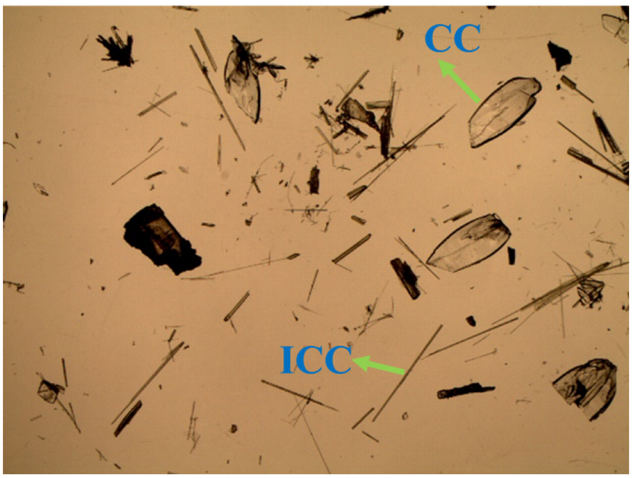

Fig. 1 Concomitant multicomponent crystals of the CC (ACA–BPY; plate-shaped) and ICC (ACA^-–BPY^+–ACA; needle-shaped).

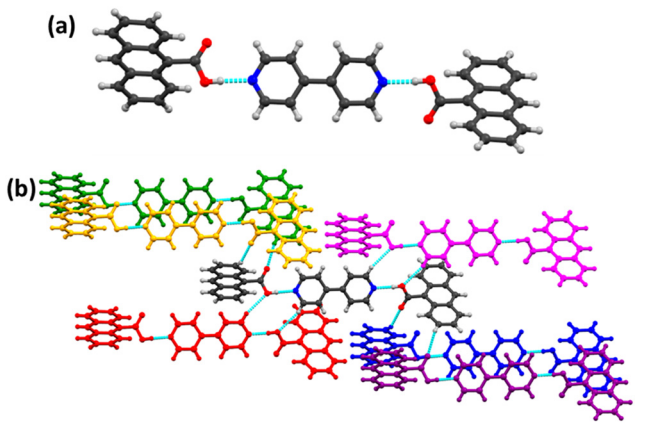

Fig. 2 Crystal structure of ACA-BPY (CC): (a) ACA and BPY molecules form a trimeric motif mediated by the acid–pyridine heterosynthon; (b) each trimeric motif is connected with six different supramolecular motifs (presented in different colors) by C–H···O interactions.

extensive network of π···π interactions (Table S3) consolidates further the crystal packing. With respect to the non-covalent interactions present, particularly N–H···O hydrogen bonds and C–H···O contacts in the ACA–BPY (2 : 1), this structure is comparable with a previously reported 1 : 1 cocrystal formed between [9,9′-bianthracene]-10,10′-dicarboxylic acid and BPY (CCDC refcode: ROWHET).[57] However, for the ROWHET structure, the dicarboxylic acid contains two carboxylic acid groups, each forming N–H···O hydrogen bonds with different BPY molecules, leading to a one-dimensional hydrogen-bonded chain further stabilized by C–H···O interactions. In contrast, ACA has only one carboxylic acid group, resulting in a discrete trimeric assembly with BPY through hydrogen bonding. This difference in the number of acid functionalities significantly influences the dimensionality and topology of the resulting supramolecular architectures (Table 1).

Crystal structures of ACA^-–BPY^+–ACA (1 : 1 : 1)

The molecular ionic cocrystal[58] ACA^-–BPY^+–ACA (ICC) crystalizes in the triclinic $P\bar{1}$ space group (Z = 2) with one ACA anion, one monoprotonated BPY and one neutral ACA molecules in the asymmetric unit (Fig. S4). Proton transfer from ACA to BPY is confirmed from the electron density map and bond length analysis [O···H (Å), θ/°: 1.61(5), 171; Table S1]. Here, the oxygen atom of the CO_2^- group of the ACA anion is involved in the bifurcated hydrogen bond with the monoprotonated BPY and ACA molecules (Fig. 3a). The carboxylate oxygen interacts with the pyridinium cation and carboxylic acid *via* N–H···O [O···N (Å), θ/°: 2.578(3), 171; Table S1] and O–H···O [O···N (Å), θ/°: 2.516(3), 168; Table S1] hydrogen bonds respectively, to form a three component supramolecular assembly. The adjacent trimeric motifs are assembled into a 2D layer (Fig. 2b) *via* C–H···O [O···C (Å), θ/°: 3.394(3), 141; 3.248(4), 150; 3.397(4), 172] and C–H···N [N···C (Å), θ/°: 3.580, 152] interactions. The 2D layers are further stabilized by π···π interactions (3.58–4.16 Å; Table S4).

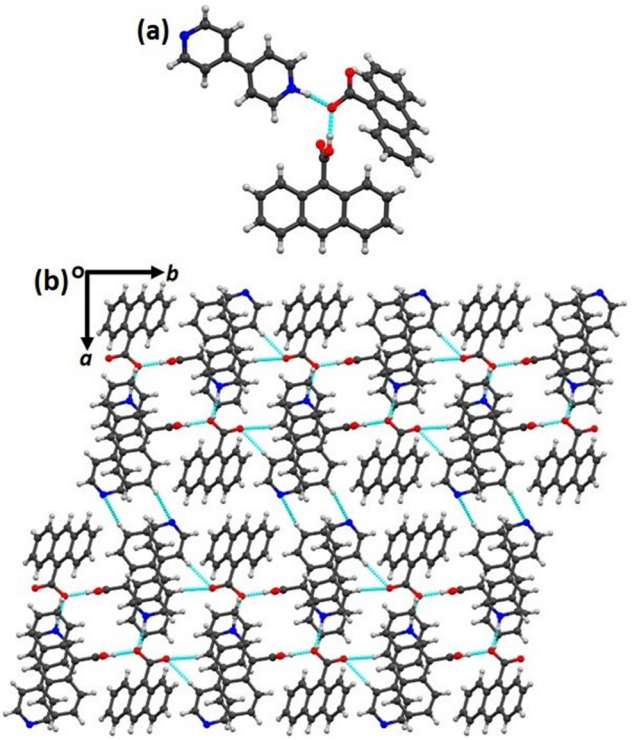

Fig. 3 Crystal structure of ACA^-–BPY^+–ACA (ICC): (a) supramolecular trimeric motif formed by H-bonding between the anthracenecarboxylate anion, monoprotonated 4,4′-bipyridine and anthracenecarboxylic acid molecules; (b) trimeric motifs are connected with each other by C–H···O and C–H···O interactions to form a 2D layer.

Table 1 Crystallographic and structural refinement parameters of cocrystal ACA–BPY (CC) and molecular ionic cocrystal ACA^-–BPY^+–ACA (ICC)

Compound name	ACA–BPY (CC)	ACA^-–BPY^+–ACA (ICC)
Temperature (K)	150 K	150 K
Formula	$C_{20}H_{14}O_2N$	$C_{40}H_{28}O_4N_2$
Formula weight	300.32	600.64
Crystal system	Monoclinic	Triclinic
Space group	$C2/c$	$P\bar{1}$
a/Å	23.3375(12)	6.8429(6)
b/Å	10.3912(5)	12.8769(12)
c/Å	12.0372(6)	17.6451(16)
α/°	90	106.325(4)
β/°	95.933(2)	99.108(4)
γ/°	90	96.639(5)
V/Å^3	2903.4(3)	1452.1(2)
Z	8	2
D_c/g cm^{-3}	1.374	1.374
μ/mm^{-1}	0.089	0.089
F(000)	1256	628
θ range/°	2.7–28.4	2.4–28.4
Reflections collected	23 109	36 515
Unique reflections	3613	7260
Reflections $I > 2\sigma(I)$	3139	4172
R_{int}	0.035	0.159
Goodness of fit (F^2)	1.08	1.03
R_1 ($I > 2\sigma(I)$)	0.0444,	0.0868
wR_2 ($I > 2\sigma(I)$)	0.1276	0.1858
CCDC no.	2446162	2446161

Hirshfeld surface analysis

Hirshfeld analysis[59] offers a pictorial identification of the characteristic noncovalent interactions and close contacts throughout the structure. The intermolecular interactions in the CC and ICC are differentiated by Hirshfeld surface (Fig. S5) and 2D fingerprint plot analysis (Fig. 4) using Crystal Explorer 3.1. The relative contribution of the important intermolecular contacts in both multicomponent solids are displayed in Fig. 4c. For both solids, the most significant contributions (>80%) come from C···H, H···H and C···C contacts, which correspond to the C–H···π /π···π contacts and van der Waals interactions, respectively. Total contribution from strong hydrogen bonding interactions N···H and O···H together is less than 20% in the crystal packing of both solids (Fig. 4). As was noticed from the single crystal X-ray diffraction analysis, Hirshfeld surface analysis also suggests

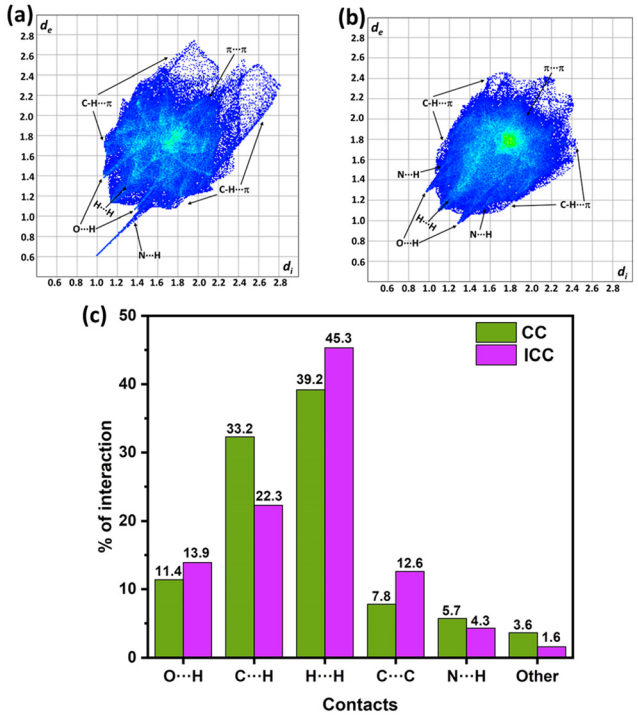

Fig. 4 (a and b) 2D fingerprint plots for the cocrystal ACA–BPY (CC) and molecular ionic cocrystal ACA^{-}–BPY^{+}–ACA (ICC); (c) relative contributions of various interactions in the CC and ICC from Hirshfeld surface analysis.

that while the strong hydrogen bonds take a primary role in the formation of the multicomponent solids, van der Waals and C–H···π/π···π interactions play a major role in guiding the three-dimensional assembly.

To identify the thermodynamically favored multicomponent form, aqueous slurry experiments were performed by slurrying the CC form in water for 7 days. Powder X-ray diffraction analysis of the dried solids revealed complete transformation to the ICC form, indicating that the ICC is thermodynamically more stable than the CC form. This conclusion is further corroborated by DTA, which shows that the ICC form exhibits a melting point 2 °C higher than that of the CC (Fig. S2). The enhanced stability of the ICC form can be rationalized structurally by the presence of charged species within the crystal lattice, as well as a greater number of stabilizing intermolecular interactions compared to the CC form.

Mechanochemical synthesis and *in situ* monitoring

The pure multicomponent solid form of ACA and BPY was synthesized *via* an environmentally sustainable mechanochemical approach, minimizing solvent usage (Fig. 5). Specifically, neat grinding (without solvent) and solvent-assisted grinding (using minimal water and conventional organic solvents) were employed. To further understand the influence of mechanochemical conditions on the ACA + BPY co-crystallization process, we monitored the reaction in real-time using TRIS-PXRD, providing crucial insights into phase evolution and reaction dynamics (Fig. 5).

Neat grinding of stoichiometric mixtures of ACA and BPY under ambient conditions resulted in time-dependent phase evolution (Fig. 5a). After 5 minutes of milling, the kinetic form, CC, was predominantly obtained, although traces of unreacted starting materials were still detectable. Extending the grinding duration to 30 minutes led to the formation of a mixture of CC and thermodynamically favored ICC forms. Interestingly, prolonged grinding for 60 minutes yielded exclusively the ICC form, with no detectable presence of the CC phase or starting components, suggesting a complete and selective solid-state transformation driven by mechanical activation (Fig. 5a). The TRIS XRD data for neat grinding of ACA with BPY reveal that reflections corresponding to the CC form begin to emerge within 40 seconds, alongside those of unreacted starting materials (Fig. 5d). With continued ball milling, reflections of the ICC form appear after 4 minutes, while those of the CC form and starting materials vanish, indicating a complete phase transformation.

Liquid-assisted grinding of ACA and BPY in the presence of water led to the formation of both kinetic CC and thermodynamic ICC forms within 5 minutes of milling (Fig. 5b). Upon continued grinding, a gradual transformation was observed. The intensity of reflections corresponding to the CC form progressively decreased over time, while those of the ICC form increased. After 30 and 60 minutes, the CC phase was still detectable but significantly diminished. Strikingly, after 120 minutes of grinding, only the thermodynamically favored ICC form was observed, with no detectable traces of the CC phase (Fig. 5b). In the TRIS experiment, reflections corresponding to both the CC and ICC forms were detected at the early stages of milling (Fig. 5e). However, as the reaction progressed, the intensity of the CC reflections gradually diminished, and by approximately 8 minutes, only reflections of the thermodynamically stable ICC form remained, signifying a complete transformation to the ICC phase. The observed differences in time-dependent phase evolution during neat grinding and water-assisted grinding between the conventional ball milling experiments and TRIS measurements can be attributed to the significantly lower quantities of reactants and the use of different milling jars used in the TRIS experiment. This reduced scale likely facilitates more efficient energy transfer and accelerated phase transformation, leading to faster and more complete conversion under TRIS conditions.

In contrast, liquid-assisted grinding with various organic solvents, including methanol, THF, acetonitrile, dioxane, and hexanol, resulted exclusively in the formation of the kinetic CC form within 5 minutes (Fig. 5 and S6). Notably, no further phase evolution was observed upon prolonged grinding. TRIS PXRD of liquid-assisted grinding with methanol revealed the appearance of reflections corresponding to the CC form as early as 20 seconds into milling, accompanied by only minor traces of the starting materials. By 40 seconds, all reflections

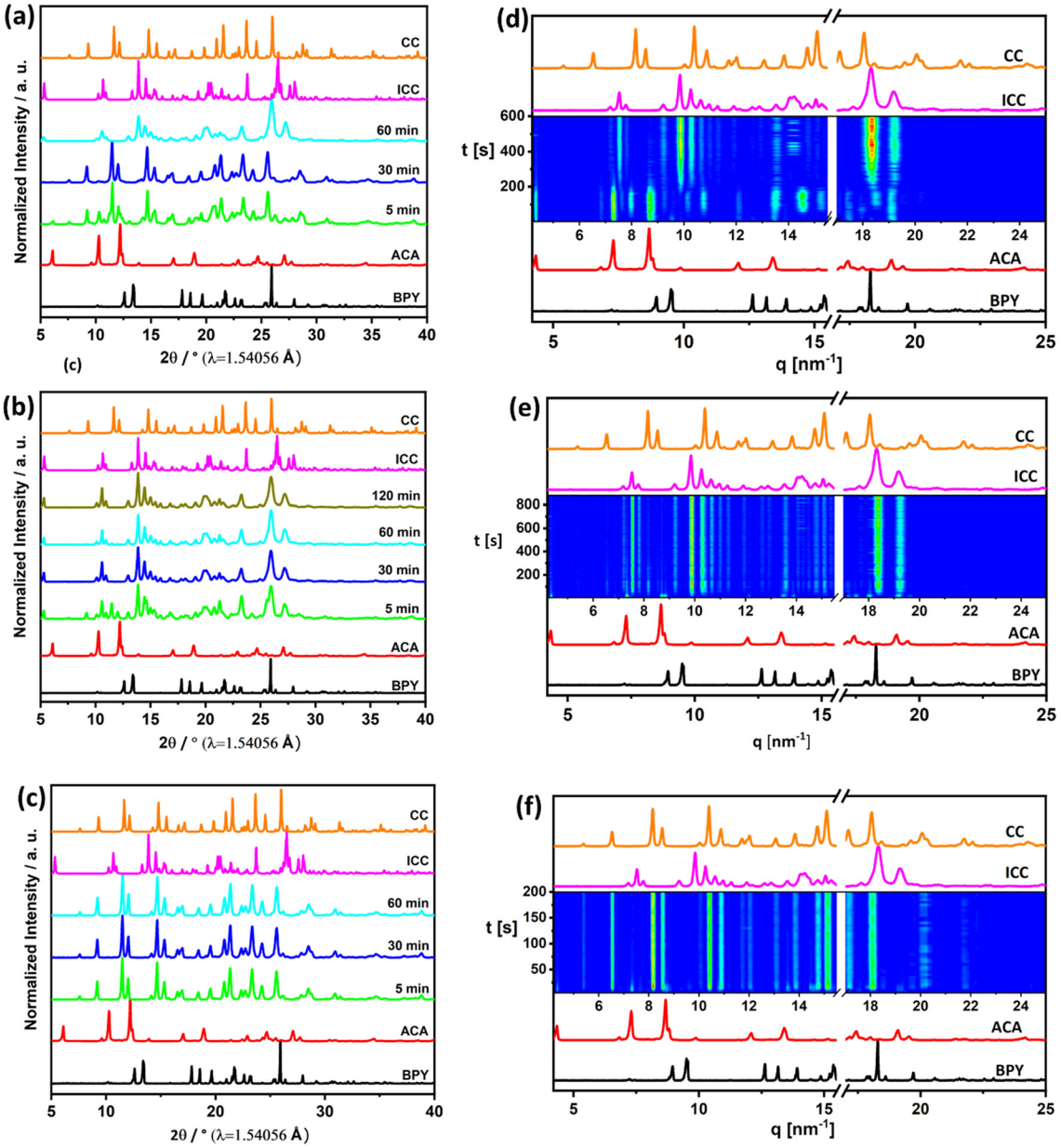

Fig. 5 PXRD patterns obtained from the milling of ACA and BPY at different time intervals under (a) neat grinding and liquid-assisted grinding using (b) water and (c) methanol. Time-resolved *in situ* powder X-ray diffraction (TRIS-PXRD) patterns of the mechanochemical reaction between ACA and BPY under (d) neat grinding and liquid-assisted grinding using (e) water and (f) methanol. The experimental patterns are compared with simulated patterns derived from single-crystal data of the corresponding cocrystal (CC, orange) and ionic cocrystal (ICC, magenta) multicomponent forms. The data in (d), (e), and (f) have been excluded in the range of 16–17 q [nm^{-1}] due to artifacts arising from synchrotron data processing.

associated with the unreacted components had disappeared, and only the kinetic CC phase remained. This phase persisted unchanged even upon prolonged milling, indicating rapid and selective formation of the CC form under these solvent conditions.[60] The milling experiments described above clearly demonstrate that the mechanochemical formation of different MOSs is strongly influenced by the choice of solvent. Analysis of the crystal structures reveals that the CC form is neutral, while the ICC form is charged. It is well-established that highly polar solvents, such as water, preferentially stabilize ionic species, whereas organic solvents, being less polar, tend to favor the stabilization of neutral compounds (Table S5). This behavior is consistently reflected in our mechanochemical experiments. All organic solvents led exclusively to the formation of the neutral kinetic CC form, with no detectable reflections corresponding to the ICC form, regardless of whether the reactions were performed in large jars with greater reactant quantities or in smaller jars with lower quantities. In contrast, liquid-assisted grinding using water initially yielded a mixture of kinetic CC

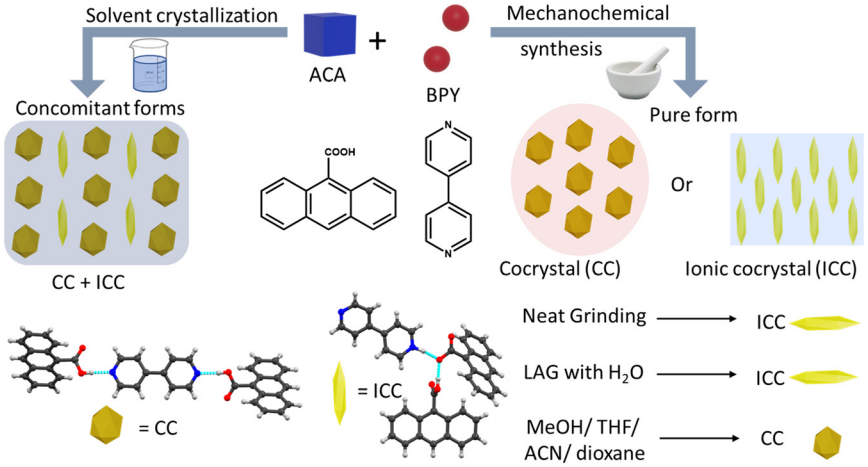

Scheme 1 Schematic presentation of the formation of MOSs of 9-anthracenecarboxylic acid (ACA) and 4,4′-bipyridine (BPY) as a mixture of two concomitant forms by solvent crystallization (left side) *vs.* pure form *via* mechanochemical synthesis (right).

and thermodynamically favored ICC forms. Over time, the CC phase gradually diminished, ultimately giving way to complete conversion to the ICC form. This is attributed to the strong stabilizing effect of water on the ionic thermodynamic ICC form. Under neat grinding conditions, without the intentional addition of solvent, both CC and ICC forms emerged initially, but prolonged grinding again led to the disappearance of the CC form and the progressive dominance of the thermodynamically favored ICC phase, culminating in full conversion to the ionic product.

Conclusion

In this study, we demonstrate that the mechanochemical approach provides a robust and selective pathway for the synthesis of multicomponent organic solids from 9-anthracenecarboxylic acid and 4,4′-bipyridine. While conventional solution crystallization consistently yields concomitant formation of neutral (CC) and ionic (ICC) cocrystals, mechanochemical methods allow for selective and phase-pure access to either form, governed by the choice of solvent and grinding conditions (Scheme 1). TRIS-PXRD revealed that water, due to its high polarity, promotes complete conversion to the thermodynamically stable ICC, while comparatively less polar organic solvents favor the formation of the neutral CC form. Notably, even under neat grinding, a time-dependent phase transformation of the kinetic CC form to thermodynamically favorable ICC form was observed. These findings highlight the ability of mechanochemistry, in conjunction with *in situ* monitoring, to steer solid-state reaction pathways and enable controlled synthesis of functional materials with desired phase and composition. This solvent-dependent selectivity offers a sustainable and scalable route for producing phase-pure multicomponent crystalline solids with tunable properties.

Author contributions

The manuscript was written through contributions of all authors. All authors have given approval to the final version of the manuscript.

Conflicts of interest

The authors declare no competing financial interest.

Data availability

Supplementary information: Fourier-transform infrared spectroscopy, thermal study, single crystal X-ray diffraction data, Hirshfeld surface analysis, powder X-ray diffraction. See DOI: **https://doi.org/10.1039/D5CE00663E**.

CCDC 2446161 and 2446162 contain the supplementary crystallographic data for this paper.[61]

Acknowledgements

The authors thank BESSY II (Helmholtz Zentrum Berlin) for beam time.

References

1 N. A. Mir, R. Dubey and G. R. Desiraju, *Acc. Chem. Res.*, 2019, **52**, 2210–2220.
2 E. Grothe, H. Meekes, E. Vlieg, J. H. Ter Horst and R. De Gelder, *Cryst. Growth Des.*, 2016, **16**, 3237–3243.
3 O. N. Kavanagh, D. M. Croker, G. M. Walker and M. J. Zaworotko, *Drug Discovery Today*, 2019, **24**, 796–804.
4 D. J. Berry and J. W. Steed, *Adv. Drug Delivery Rev.*, 2017, **117**, 3–24.
5 G. Bolla, B. Sarma and A. K. Nangia, *Chem. Rev.*, 2022, **122**, 11514–11603.
6 X. Wang, Z. Wang, X. Wang, F. Kang, Q. Gu and Q. Zhang, *Angew. Chem.*, 2024, **136**, e202416181.

7 A. S. Mahadevi and G. N. Sastry, *Chem. Rev.*, 2016, **116**, 2775–2825.
8 L. Sun, Y. Wang, F. Yang, X. Zhang and W. Hu, *Adv. Mater.*, 2019, **31**, 1902328.
9 P. P. Mazzeo, M. Pioli, F. Montisci, A. Bacchi and P. Pelagatti, *Cryst. Growth Des.*, 2021, **21**, 5687–5696.
10 M. Djaló, A. E. S. Cunha, J. P. Luís, S. Quaresma, A. Fernandes, V. André and M. T. Duarte, *Cryst. Growth Des.*, 2021, **21**, 995–1005.
11 G. Springuel, B. Norberg, K. Robeyns, J. Wouters and T. Leyssens, *Cryst. Growth Des.*, 2012, **12**, 475–484.
12 F. Montisci, P. P. Mazzeo, C. Carraro, M. Prencipe, P. Pelagatti, F. Fornari, F. Bianchi, M. Careri and A. Bacchi, *ACS Sustainable Chem. Eng.*, 2022, **10**, 8388–8399.
13 R. Rathi, S. Kaur and I. Singh, *Cryst. Growth Des.*, 2022, **22**, 2023–2042.
14 I. Nyamba, C. B. Sombié, M. Yabré, H. Zimé-Diawara, J. Yaméogo, S. Ouédraogo, A. Lechanteur, R. Semdé and B. Evrard, *Eur. J. Pharm. Biopharm.*, 2024, **204**, 114513.
15 M. K. C. Mannava, A. Gunnam, A. Lodagekar, N. R. Shastri, A. K. Nangia and K. A. Solomon, *CrystEngComm*, 2021, **23**, 227–237.
16 O. N. Kavanagh, D. M. Croker, G. M. Walker and M. J. Zaworotko, *Drug Discovery Today*, 2019, **24**, 796–804.
17 H.-Y. Liu, Y.-C. Li and X.-D. Wang, *CrystEngComm*, 2023, **25**, 3126–3141.
18 D. Barman, D. Barman, K. Bhattacharyya and P. K. Iyer, *Adv. Opt. Mater.*, 2024, **12**, 2401352.
19 W. Wang, L. Luo, Z. Lin, Z. Mu, Z. Ju, B. Yang, Y. Li, M. Lin, G. Long, J. Zhang, J. Zhao and W. Huang, *J. Mater. Chem. C*, 2021, **9**, 7928–7935.
20 A. A. Dar and S. Rashid, *CrystEngComm*, 2021, **23**, 8007–8026.
21 J. C. Bennion and A. J. Matzger, *Acc. Chem. Res.*, 2021, **54**, 1699–1710.
22 S. Hanafi, D. Trache, R. Meziani, H. Boukciat, A. Mezroua, A. F. Tarchoun and M. Derradji, *Chem. Eng. J.*, 2021, **417**, 128010.
23 R. V. Kent, R. A. Wiscons, P. Sharon, D. Grinstein, A. A. Frimer and A. J. Matzger, *Cryst. Growth Des.*, 2018, **18**, 219–224.
24 L. Sun, W. Zhu, X. Zhang, L. Li, H. Dong and W. Hu, *J. Am. Chem. Soc.*, 2021, **143**, 19243–19256.
25 M. Malamatari, S. A. Ross, D. Douroumis and S. P. Velaga, *Adv. Drug Delivery Rev.*, 2017, **117**, 162–177.
26 N. Thakur, M. Prashar, S. Kaur, N. Dhingra, M. Kumar, R. Rathi, I. Singh and P. Arora, in *Cocrystals in Pharmaceutical Sciences*, ed. I. Singh, S. Mallick and R. Rathi, Wiley, 1st edn, 2025, pp. 93–120.
27 K. Fucke, S. A. Myz, T. P. Shakhtshneider, E. V. Boldyreva and U. J. Griesser, *New J. Chem.*, 2012, **36**, 1969.
28 J. H. T. Horst and P. W. Cains, *Cryst. Growth Des.*, 2008, **8**, 2537–2542.
29 S. Aitipamula, P. S. Chow and R. B. H. Tan, *CrystEngComm*, 2014, **16**, 3451.
30 C. Yao, S. Zhang, L. Wang and X. Tao, *Cryst. Growth Des.*, 2023, **23**, 637–654.
31 A. Bērziņš, A. Trimdale-Deksne, S. Belyakov and J. H. Ter Horst, *Cryst. Growth Des.*, 2023, **23**, 5469–5476.
32 S. Kumar, O. Prakash, A. Gupta and S. Singh, *Curr. Org. Synth.*, 2019, **16**, 385–397.
33 I. R. Speight, K. J. Ardila-Fierro, J. G. Hernández, F. Emmerling, A. A. L. Michalchuk, F. García, E. Colacino and J. Mack, *Nat. Rev. Methods Primers*, 2025, **5**, 29.
34 A. Bodach, A. Portet, F. Winkelmann, B. Herrmann, F. Gallou, E. Ponnusamy, D. Virieux, E. Colacino and M. Felderhoff, *ChemSusChem*, 2024, **17**, e202301220.
35 A. A. L. Michalchuk, E. V. Boldyreva, A. M. Belenguer, F. Emmerling and V. V. Boldyrev, *Front. Chem.*, 2021, **9**, 685789.
36 T. Friščić, C. Mottillo and H. M. Titi, *Angew. Chem., Int. Ed.*, 2020, **59**, 1018–1029.
37 L. Wang, G. Sun, K. Zhang, M. Yao, Y. Jin, P. Zhang, S. Wu and J. Gong, *ACS Sustainable Chem. Eng.*, 2020, **8**, 16781–16790.
38 F. Fischer, S. Greiser, D. Pfeifer, C. Jäger, K. Rademann and F. Emmerling, *Angew. Chem., Int. Ed.*, 2016, **55**, 14281–14285.
39 O. Bento, F. Luttringer, T. Mohy El Dine, N. Pétry, X. Bantreil and F. Lamaty, *Eur. J. Org. Chem.*, 2022, **2022**, e202101516.
40 T. Stolar, S. Grubešić, N. Cindro, E. Meštrović, K. Užarević and J. G. Hernández, *Angew. Chem., Int. Ed.*, 2021, **60**, 12727–12731.
41 D. Braga, L. Maini and F. Grepioni, *Chem. Soc. Rev.*, 2013, **42**, 7638.
42 C. Bolm, R. Mocci, C. Schumacher, M. Turberg, F. Puccetti and J. G. Hernández, *Angew. Chem., Int. Ed.*, 2018, **57**, 2423–2426.
43 M. Ferguson and T. Friščić, *Phys. Chem. Chem. Phys.*, 2024, **26**, 9940–9947.
44 Z. X. Ng, D. Tan, W. L. Teo, F. León, X. Shi, Y. Sim, Y. Li, R. Ganguly, Y. Zhao, S. Mohamed and F. García, *Angew. Chem., Int. Ed.*, 2021, **60**, 17481–17490.
45 I. Akhmetova, M. Rautenberg, C. Das, B. Bhattacharya and F. Emmerling, *ACS Omega*, 2023, **8**, 16687–16693.
46 M. Rautenberg, B. Bhattacharya, J. Witt, M. Jain and F. Emmerling, *CrystEngComm*, 2022, **24**, 6747–6750.
47 P. A. Julien, M. Arhangelskis, L. S. Germann, M. Etter, R. E. Dinnebier, A. J. Morris and T. Friščić, *Chem. Sci.*, 2023, **14**, 12121–12132.
48 A. A. L. Michalchuk and F. Emmerling, *Angew. Chem., Int. Ed.*, 2022, **61**, e202117270.
49 S. Lukin, L. S. Germann, T. Friščić and I. Halasz, *Acc. Chem. Res.*, 2022, **55**, 1262–1277.
50 A. Guilherme Buzanich, C. T. Cakir, M. Radtke, M. B. Haider, F. Emmerling, P. F. M. De Oliveira and A. A. L. Michalchuk, *J. Chem. Phys.*, 2022, **157**, 214202.
51 G. I. Lampronti, A. A. L. Michalchuk, P. P. Mazzeo, A. M. Belenguer, J. K. M. Sanders, A. Bacchi and F. Emmerling, *Nat. Commun.*, 2021, **12**, 6134.
52 P. F. M. De Oliveira, A. A. L. Michalchuk, A. G. Buzanich, R. Bienert, R. M. Torresi, P. H. C. Camargo and F. Emmerling, *Chem. Commun.*, 2020, **56**, 10329–10332.

53 K. J. Ardila-Fierro and J. G. Hernández, *Angew. Chem., Int. Ed.*, 2024, **63**, e202317638.
54 G. M. Sheldrick, *Acta Crystallogr., Sect. A:Found. Crystallogr.*, 2008, **64**, 112–122.
55 G. M. Sheldrick, *SADABS, A Software for Empirical Absorption Correction (version Version 2.05)*, University of Göttingen, Göttingen, 2002.
56 G. M. Sheldrick, *Acta Crystallogr., Sect. C:Struct. Chem.*, 2015, **71**, 3–8.
57 M. Okayasu, S. Kikkawa, H. Hikawa and I. Azumaya, *CrystEngComm*, 2020, **22**, 497–505.
58 C. O'Malley, P. McArdle and A. Erxleben, *Cryst. Growth Des.*, 2022, **22**, 3060–3071.
59 M. A. Spackman and D. Jayatilaka, *CrystEngComm*, 2009, **11**, 19–32.
60 Y. Marcus, *The Properties of Solvents*, John Wiley and Sons, Ltd., England, 1999.
61 (*a*) T. Feiler, F. Emmerling and B. Bhattacharya, CCDC 2446161: Experimental Crystal Structure Determination, 2025, DOI: **10.5517/ccdc.csd.cc2n3ffn**; (*b*) T. Feiler, F. Emmerling and B. Bhattacharya, CCDC 2446162: Experimental Crystal Structure Determination, 2025, DOI: **10.5517/ccdc.csd.cc2n3fgp**.